Geoscience Frontiers 16 (2025) 102169

Contents lists available at ScienceDirect

Geoscience Frontiers

journal homepage: www.elsevier.com/locate/gsf

Research Paper

Noble gas constraints on fluid flow and hydrocarbon accumulation in the Yinggehai Basin, Northwestern South China Sea

Rui Liu [a], Rui Xu [a], Tao Wen [b,*], Khi Atchinson [b], Ziqi Feng [c], Fang Hao [c], Lin Hu [d], Jinqiang Tian [c], Yazhen Zhang [d], Jianzhang Liu [e], Lei Tuo [d]

[a] *School of Geoscience and Technology, Southwest Petroleum University, Chengdu 610500, China*
[b] *Department of Earth and Environmental Sciences, Syracuse University, Syracuse, NY 13244, United States*
[c] *School of Geosciences, China University of Petroleum, Qingdao 266580, China*
[d] *Haikou Branch of CNOOC Limited, Haikou 570312, China*
[e] *Key Laboratory of Tectonics and Petroleum Resources (China University of Geosciences), Ministry of Education, Wuhan 430074, China*

ARTICLE INFO

Article history:
Received 26 March 2025
Revised 7 September 2025
Accepted 26 September 2025
Available online 29 September 2025

Keywords:
Yinggehai Basin
Hydrocarbon accumulation
Noble gas geochemistry
Source tracing
Fluid leakage
Fluid migration

ABSTRACT

Multiple physicochemical processes involving organic and inorganic components may alter hydrocarbon composition and isotopic signatures, posing a challenge in accurately tracing natural gas accumulation. In contrast, noble gases are chemically inert and highly sensitive to fluid flow processes, offering a powerful tool for precisely tracing natural gas accumulation. By analyzing and modeling noble gas geochemistry data of gas samples from gas fields in the Yinggehai Basin, South China Sea, we constrained fluid flow patterns and traced the natural gas accumulation process. In particular, the low $^{3}He/^{4}He$ and high $^{40}Ar/^{36}Ar$ values of gas samples suggested atmospheric-crustal mixing, with the suspected central fault significantly influencing the $^{40}Ar^{*}$ (* denotes crustal noble gas) proportion and $^{40}Ar/^{36}Ar$ value in charging fluids. Binary mixing of atmospheric and crustal noble gases elevated the $^{40}Ar^{*}/^{4}He^{*}$ value in well-preserved gas fields. Diapir activity and/or long-term artificial extraction had likely promoted noble gas leakage which further elevated the $^{40}Ar^{*}/^{4}He^{*}$ to abnormally high levels. Three key time windows for $^{4}He^{*}$ accumulation, i.e., 4–4.5 Ma, 1–2 Ma, and 0–0.5 Ma, were identified in well-preserved gas fields. The suspected central fault facilitated the migration of both high $^{40}Ar/^{36}Ar$ fluids and highly mature hydrocarbons characterized by heavier $\delta^{13}C_1$ and high $C_1/C_{1\text{-}5}$ ratios. In most gas fields, methane (C_1) migration was dominated by the gas phase, as indicated by the high $C_1/^{36}Ar$ value. However, in a few leaked or shallow-buried gas fields, low $C_1/^{36}Ar$ ratios suggest that C_1 also migrated with water. The duration of trap sealing and the depth of the transport system played critical roles in hydrocarbon accumulation. Longer trap sealing and greater transport system depth favored hydrocarbons derived from the Lower Miocene Sanya Formation. In contrast, shorter trap sealing durations and limited transport system depth led to the accumulation of hydrocarbons sourced from the Middle Miocene Meishan Formation.

1. Introduction

Noble gases (He, Ne, Ar, Kr, Xe) are chemically inert and ubiquitously present in nature, making them ideal natural tracers for investigating geological fluid flow processes (Ballentine and Burnard, 2002). Furthermore, hydrocarbon-associated noble gases have been used to qualitatively or quantitatively analyze critical processes of hydrocarbon accumulation (Hunt et al., 2012; Chen et al., 2023), source (Ballentine et al., 1991) and migration tracing (Battani et al., 2000; Byrne et al., 2020), accumulation dating (Zhou and Ballentine, 2006; Barry et al., 2017), and hydrocarbon adjustment (or redistribution) (Barry et al., 2016; Brown, 2019; Li et al., 2020; Karolytė et al., 2021; Chen et al., 2022).

Noble gases in hydrocarbon reservoirs originate from three primary sources: atmosphere, crust, and mantle (Wen et al., 2015, 2016, 2017; Tolstikhin et al., 2017; Byrne et al., 2018, 2020; Li et al., 2022). Atmospheric-derived noble gases enter deep subsurface strata through atmospheric fluid recharge and infiltration (i.e., air-saturated water, ASW). These atmosphere-derived noble gases have characteristic elemental and isotopic ratios (e.g., $^{20}Ne/^{36}Ar$, $^{84}Kr/^{36}Ar$, $^{132}Xe/^{36}Ar$) which can be altered by solubility-driven fractionation in multiphase fluids (water/oil/gas) (Battani and Prinzhofer, 2000; Zhou et al., 2005; Gilfillan et al.,

---

* Corresponding author.
E-mail address: twen08@syr.edu (T. Wen).

https://doi.org/10.1016/j.gsf.2025.102169
1674-9871/

2008). Crust-derived noble gases (e.g., ^{4}He*, ^{21}Ne*, ^{40}Ar*) are generated by radiogenic or nucleogenic reactions of elements (e.g., U, Th, K, O, and Mg) in crustal rocks. The elemental ratios of crust-derived noble gases (e.g., ^{4}He*/^{40}Ar*, ^{4}He*/^{21}Ne*, ^{21}Ne*/^{40}Ar*) are controlled by both the elemental composition of the parent rocks and their closure temperatures. In particular, ^{4}He* and ^{21}Ne* are released from mica and feldspar minerals at relatively low closure temperatures (50–70 °C), while ^{40}Ar* is released at 230–300 °C (Ballentine et al., 1994; Snee, 2002). Metamorphic or volcanic events, along with tectonic deformation, can promote the release of crust-derived noble gases from host minerals into pore fluids through thermal and mechanical processes. Mantle-derived noble gases (e.g., He) are typically rare in shallow crustal fluids, except in regions experiencing crustal thinning (e.g., mid-ocean ridges), volcanic or tectonic activities (Kennedy and van Soest, 2007; Horiguchi and Matsuda, 2013; Pinti et al., 2013; Han et al., 2022).

Noble gas signatures (atmospheric, crustal, and mantle-derived) exhibit pronounced spatial and temporal correlations with tectonic processes, which can directly infer the migration and preservation conditions of multi-sourced fluids (Liu et al., 2021, 2025). At continental scales, deformation-enhanced permeability of the lithosphere explains the westward increase of ^{3}He/^{4}He ratios across western North American, which aligns with elevated tectonic strain rates (Kennedy and van Soest, 2007). Similarly, laboratory triaxial deformation experiments demonstrate enhanced release of radiogenic ^{4}He* and ^{40}Ar* during rock dilation and macroscopic failure under high confining pressures (Bauer et al., 2016). In summary, noble gas elemental or isotope ratios are sensitive tracers of tectonically mediated fluid-rock interactions across geological timescales.

The Yinggehai Basin, located on the northwestern margin of the South China Sea, is one of the most petroliferous basins. Previous fluid geochemistry research in this basin has primarily focused on the stable carbon and oxygen isotopes of hydrocarbons (Huang et al., 2005, 2015; Lin et al., 2024; Xie and Huang, 2014). However, these isotopic signatures can be significantly altered by various physicochemical processes during hydrocarbon generation, migration, and preservation promoted by tectonic evolution, making it challenging to achieve consensus on the charging-controlled (Huang et al., 2005, 2015; Xie and Huang, 2014) and leakage-induced (Liu et al., 2018, 2019; Lin et al., 2024; Chen et al., 2025) variations in hydrocarbon accumulation processes. In this study, we aim to leverage the unique geochemical characteristics of noble gases to gain new insights into fluid flow and hydrocarbon accumulation processes in the Yinggehai Basin. These findings could ultimately contribute to more effective hydrocarbon exploration and production strategies in similar geological settings.

2. Geological settings

The Yinggehai Basin is located west of Hainan Island (China) and east of the Indochina Plate. It has a distinctive rhombic-shape with a pronounced NNW–SSE orientation (Fig. 1) and is primarily composed of the northern Lingao Uplift, the central Yinggehai Depression, the eastern Yingdong Slope, and the western Yingxi Slope (Fig. 1). The Moho depth of the Yinggehai Basin is approximately 22–24 km; the fluctuation of the Moho depth and the anomalies in Bouguer gravity suggest the presence of a central fault in the basin (Sun et al., 2003). Driven by the movements of

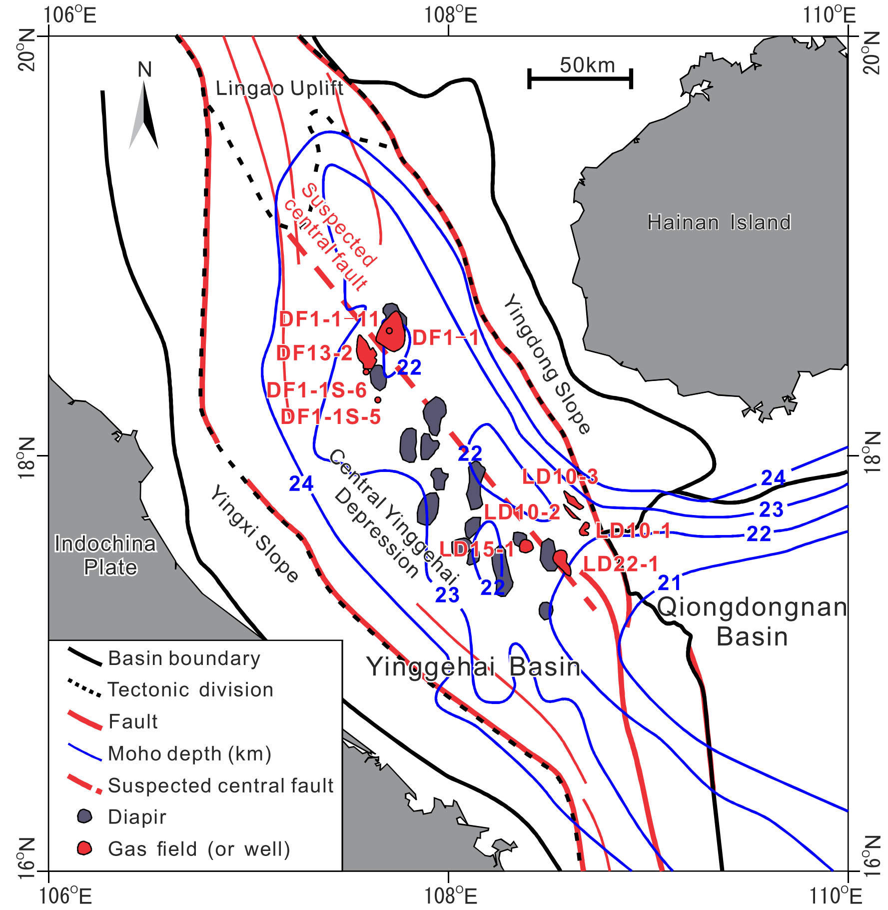

Fig. 1. Tectonic settings of the Yinggehai Basin. Moho depth is adapted from Gong and Li (1997). The suspected central fault is after Sun et al. (2003).

the Indochina Plate and the South China Plate, the central fault and the boundary fault system of the Yinggehai Basin underwent the Paleogene rifting stage, followed by a Neogene post-rift thermal subsidence stage (Fig. 2).

The Yinggehai Basin is characterized by a remarkably thick (8–16 km) sedimentary succession, consisting of the Paleogene continental fluvial-lacustrine sedimentary system formed during the rifting stage and the Neogene marine sedimentary system developed during the thermal subsidence stage. The Lower-Middle Miocene marine shale is considered as the hydrocarbon source rock (Liu et al., 2024), while the Middle-Upper Miocene deep-water channels (Jiang et al., 2022) or fans (Zhang et al., 2013; Liu et al., 2018; Dang, 2023) and the Pliocene–Quaternary offshore sandbars and deltas (Gao et al., 2021; Zhang et al., 2021) serve as the main hydrocarbon reservoirs. The Upper Miocene and Pliocene marine mudstones act as the hydrocarbon caprocks (Xie, 2019).

The Yinggehai Basin is a typical high-temperature and high-pressure basin, with an average geothermal gradient of ~ 42 °C/km (He et al., 2002; Zheng et al., 2023) and a pressure coefficient (the ratio of fluid pressure to hydrostatic pressure at equivalent depth) that can exceed 2.2 (Jiang et al., 2022). Despite the high-temperature and high-pressure conditions, more than 10 commercial gas fields, including DF1-1, LD15-1, LD22-1, DF13-1, DF13-2, LD10-1, LD10-2, and LD10-3, have been discovered in the Yinggehai Basin. The primary hydrocarbon-bearing formations, or pay zones, vary across the different gas fields (Fig. 2). The main pay zone of the LD22-1 field is the Quaternary Ledong Formation, while the DF1-1 and LD15-1 fields are dominated by the pay zone of the Pliocene Yinggehai Formation. Despite differences in the primary pay zones, the LD22-1, DF1-1, and LD15-1 gas fields are all associated with diapir structures. These diapir structures have significantly mixed the hydrocarbon gas with non-hydrocarbon components (up to 90 mol%), e.g., CO_2 and N_2 (Huang et al., 2005; Wang and Huang, 2008).

In contrast, the pay zone of the DF13-2 gas field is the Upper Miocene Huangliu Formation, which has a pressure coefficient of 1.9 and a temperature exceeding 140 °C (Zhang et al., 2013; Xie et al., 2014; Huang et al., 2015; Liu et al., 2019). Because the DF13-2 gas field is located farther from the diapir structures, the proportion of non-hydrocarbon components in its gas has been reduced to less than 30 mol%. The pay zone of the LD10-1 field is also the Huangliu Formation, while the pay zones of the LD10-2 and LD10-3 fields are the Middle Miocene Meishan Formation. Despite their greater distance from the diapir structures, the LD10-1, LD10-2, and LD10-3 fields still contain high percentages of non-hydrocarbon gas components (up to 70 mol%) with pressure coefficients of >2.2 and temperatures above 200 °C (Fan et al., 2021; Jiang et al., 2022).

3. Sample and method

3.1. Samples

This study primarily analyzed wellhead gas samples collected from production wells in DF1-1, LD15-1, LD22-1, DF13-2, and

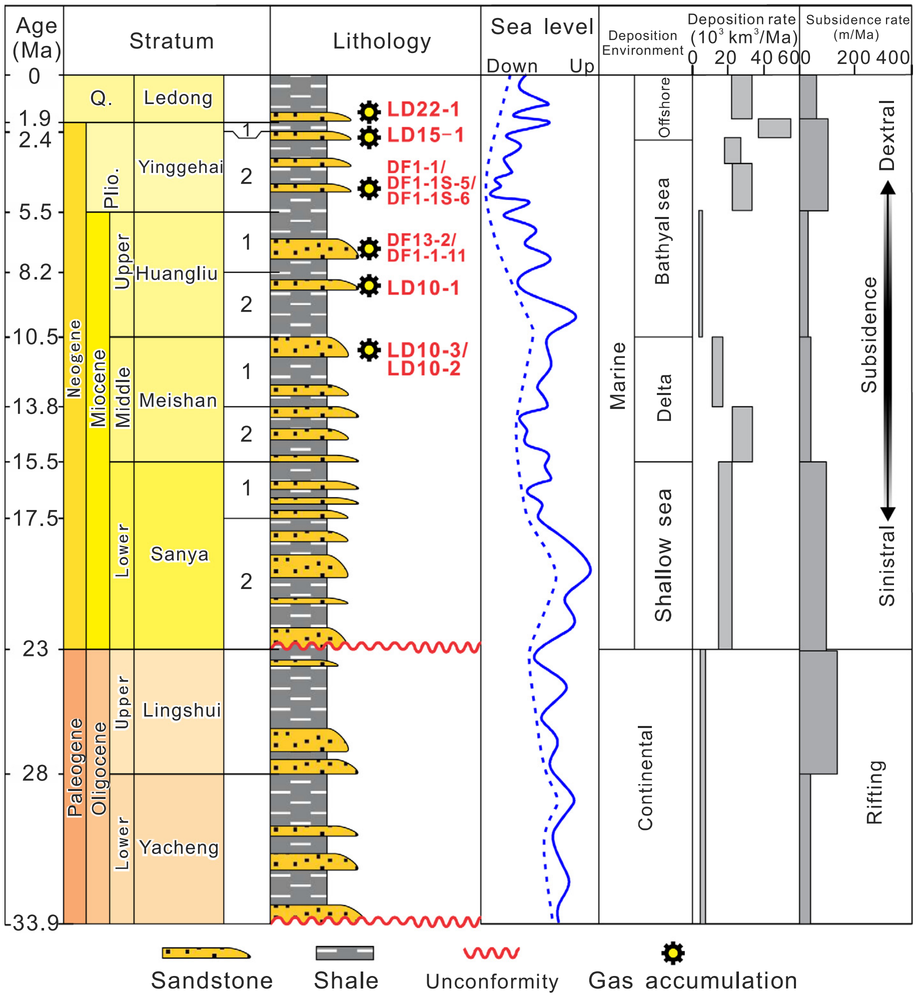

Fig. 2. Generalized lithostratigraphy of the Yinggehai Basin. The deposition rate is after Clift and Sun (2006). The tectonic subsidence rate is after Gong and Li (1997).

LD10-1 fields, as well as the in-situ DST (drill stem test) samples from LD10-2, LD10-3, DF1-1–11, DF1-1S-5, and DF1-1S-6 fields. A total of 40 samples were collected using the high-pressure steel cylinder equipped with two shut-off valves from September 2002 to November 2020, and then 37 samples sent to the Geochemistry Analytical & Testing Center (GATC), Northwest Institute of Eco-Environment and Resources, Chinese Academy of Sciences for hydrocarbon and noble gas analyses, the other 3 samples were analyzed in the Experimental Research Center (ERC) of Wuxi Research Institute of Petroleum Geology of SINOPEC (Table 1). The concentrations of He and Ar, along with the isotopic ratios of ^{3}He/^{4}He, ^{38}Ar/^{36}Ar, and ^{40}Ar/^{36}Ar are shown in Table 1.

3.2. Binary mixing of noble gases end-members

Crustal ^{4}He and ^{40}Ar (denoted as ^{4}He* and ^{40}A* respectively) were estimated from the atmosphere-crust binary mixing model of Ballentine et al. (2002):

$$^{4}\mathrm{He}^{*} = {}^{4}\mathrm{He}_{\mathrm{measured}} \times \frac{R_a - R_{\mathrm{measured}}}{R_a - R_c} \tag{1}$$

where ^{4}He$_{\mathrm{measured}}$ is the measured ^{4}He concentration (cc (STP)/cc), R_a is the ^{3}He/^{4}He of atmosphere (1.384×10^{-6} cc (STP)/cc), R_{measured} is the measured ^{3}He/^{4}He value, R_c is the ^{3}He/^{4}He value of typical crust (~0.01R_a).

$$^{40}\mathrm{Ar}^{*} = {}^{40}\mathrm{Ar}_{\mathrm{measured}} \times \left[1 - \left(\frac{^{40}\mathrm{Ar}}{^{36}\mathrm{Ar}}\right)_{\mathrm{air}} \Big/ \left(\frac{^{40}\mathrm{Ar}}{^{36}\mathrm{Ar}}\right)_{\mathrm{measured}}\right] \tag{2}$$

where ^{40}Ar$_{\mathrm{measured}}$ is the measured ^{40}Ar concentration (cc (STP)/cc), (^{40}Ar/^{36}Ar)$_{\mathrm{air}}$ is the ^{40}Ar/^{36}Ar of atmosphere (298.56 [Mark et al., 2011]), and (^{40}Ar/^{36}Ar)$_{\mathrm{measured}}$ is the measured ^{40}Ar/^{36}Ar value.

3.3. ^{4}He accumulation age and dating

Assuming a total degassing model (i.e., ^{4}He*, unaffected by solubility or diffusion fractionation, primarily degassed from brines that came in contact with rock matrix), thus ^{4}He* dissolved in brine can be estimated as (Zhou and Ballentine, 2006; Wen et al., 2015):

$$^{4}\mathrm{He}^{*}_{\mathrm{water}} = \left(\frac{^{4}\mathrm{He}^{*}}{^{36}\mathrm{Ar}_{\mathrm{measured}}}\right)_{\mathrm{gas}} \times {}^{36}\mathrm{Ar}_{\mathrm{ASW}} \tag{3}$$

where ^{4}He*$_{\mathrm{water}}$ is the ^{4}He* concentration dissolved in brine (cc (STP)/cc), (^{4}He*/^{36}Ar$_{\mathrm{measured}}$)$_{\mathrm{gas}}$ is the ratio of ^{4}He* to ^{36}Ar measured in gas samples, ^{36}Ar$_{\mathrm{ASW}}$ is the ^{36}Ar concentration in the air-saturated water (cc (STP)/cc). Whereas ^{4}He*$_{\mathrm{water}}$ can be predicated as (Zhou and Ballentine, 2006; Wen et al., 2015):

$$^{4}\mathrm{He}^{*}_{\mathrm{water}} = {}^{4}\mathrm{He}_{\mathrm{in-situ}} + {}^{4}\mathrm{He}_{\mathrm{external}} \tag{4}$$

where ^{4}He$_{\mathrm{in\text{-}situ}}$ represents the ^{4}He* generated by the in-situ radioactive decay of U and Th within the reservoir, and ^{4}He$_{\mathrm{extrernal}}$ is the ^{4}He* charged into the reservoir from an external source,

$$^{4}\mathrm{He}_{\mathrm{in-situ}} = P(^{4}\mathrm{He}) \times \rho_{\mathrm{rock}} \times \Lambda \times \left(\frac{1-\omega}{\omega}\right) \times t\mathrm{cm}^{3}\mathrm{STPg}^{-1}{}_{\mathrm{H_2O}} \tag{5}$$

where ρ_{rock} and ω are the density (g/cm^3) and porosity of reservoir rock respectively, Λ is the transfer efficiency of ^{4}He* from the reservoir rock matrix to the pore water (assumed to be 1), t is the time (years), P(^{4}He) is the in-situ generation rate of ^{4}He* which depends on the U and Th concentrations of reservoir rock matrix, i.e.,

$$P(^{4}\mathrm{He}) = 1.207 \times 10^{-13}[\mathrm{U}] + 2.867 \times 10^{-14}[\mathrm{Th}]\mathrm{cm}^{3}\mathrm{STPg}^{-1}{}_{\mathrm{rock}}\mathrm{yr}^{-1} \tag{6}$$

$$P\left(^{4}\mathrm{He}/^{40}\mathrm{Ar}\right) = \left\{\left(3.115 \times 10^{6} + 1.272 \times 10^{5}\right)[\mathrm{U}] + 7.710 \times 10^{5}[\mathrm{Th}]\right\}/102.2[\mathrm{K}] \tag{7}$$

where [U], [Th], and [K] are U, Th, and K concentrations (ppm) respectively. Assuming that ^{4}He*$_{\mathrm{external}}$ primarily sourced from upper or lower crust, i.e.,

$$^{4}\mathrm{He}_{\mathrm{external}} = P(^{4}\mathrm{He}) \times \rho_{\mathrm{crust}} \times H \times \left(\frac{1}{\omega h}\right) \times t\,\mathrm{cm}^{3}\mathrm{STPg}^{-1}{}_{\mathrm{H_2O}} \tag{8}$$

where ρ_{crust} and H are density (g/cm^3) and thickness (m) of crust respectively, and h is the reservoir thickness (m).

It is important to note that in scenarios where ^{4}He in the initial brine is not completely transferred into the gas phase or undergoes substantial fractionation, the applicability of the above age model becomes limited.

3.4. Noble gas and hydrocarbon leakage

Assuming that the movements of noble gases and hydrocarbons are coupled, hydrocarbon leakage can be simulated by modeling the fractionation of noble gases that occurs during their leakage. If the fractionation process is mass-dependent, it can be described using a mass-dependent fractionation model (Ma et al., 2009):

$$\left(\frac{i}{j}\right)_{\mathrm{retained}} = \left(\frac{i}{j}\right)_{\mathrm{initial}} \times f^{\sqrt{M_j/M_i}-1} \tag{9}$$

$$\left(\frac{i}{j}\right)_{\mathrm{escaped}} = \left(\frac{i}{j}\right)_{\mathrm{initial}} \times \frac{1-f^{\sqrt{M_j/M_i}}}{1-f} \tag{10}$$

where $(i/j)_{\mathrm{initial}}$, $(i/j)_{\mathrm{retained}}$, and $(i/j)_{\mathrm{escaped}}$ are the element or isotope ratios of initial, escaped, and residual phases, respectively, i and j are different noble gas isotopes, M_i and M_j are the isotope masses, f is the fraction of isotope j in the retained phase.

4. Results

4.1. Noble gas

He concentration in our samples ranges from 3.00×10^{-6} cc (STP)/cc to 3.86×10^{-5} cc (STP)/cc, which is well below the commercial standard of 0.3 mol% (National Research Council, 2010). Nevertheless, the ^{4}He concentration, ranging from (0.2–3.86) × 10^{-5} cc (STP)/cc, exceeds the atmospheric value of 5.24×10^{-6} cc (STP)/cc (Ozima and Podosek, 2002). The measured ^{3}He/^{4}He values vary from 1.02×10^{-8} to 6.94×10^{-8} (0.01 R_a to 0.5 R_a) (Fig. 3), where R_a is the atmospheric value of 1.386×10^{-6} (Boucher et al., 2018). DST samples show an upward increase of R/R_a (Fig. 4a).

^{36}Ar concentration in our samples varies from 1.86×10^{-8} cc (STP)/cc to 8.07×10^{-7} cc (STP)/cc, which is well below the atmospheric value of 3.142×10^{-5} cc (STP)/cc (Ozima and Podosek, 2002). The measured ^{40}Ar/^{36}Ar values generally exceed the atmospheric value of 298.56 (Mark et al., 2011), ranging from 295.6 to 1078.0 (Figs. 3 and 5). DST samples further show a progressive decrease in ^{40}Ar/^{36}Ar ratios toward shallower depths (Fig. 4b). ^{38}Ar/^{36}Ar values generally align with the atmospheric value (Fig. 3).

4.2. Hydrocarbon gas

DST samples obtained from LD10-2, LD10-3, DF1-1-11, DF1-1S-5, and DF1-1S-6 fields show methane (C$_1$) concentration ranging from 7.08 to 86.94 mol% and a dryness ratio (C$_1$/ C$_{1\text{-}5}$) of 0.81–0.97. Carbon isotope of methane (δ^{13}C-C$_1$) varies from −37.1‰ to −28.2‰ (Table 1) and generally becomes enriched with increasing burial depth (Fig. 4c), indicating the dominance of thermogenic dry gas in the samples and higher thermal maturity at greater depths.

Table 1
Location, reservoir depth, and noble gas data and hydrocarbon composition of collected gas samples.

No.	Fields (or wells)	Sample types	Sample date	Reservoirs	Depth (m)	Lab.	He ($\times 10^{-5}$)	^{3}He ($\times 10^{-12}$)	^{4}He ($\times 10^{-5}$)	^{4}He* ($\times 10^{-5}$)	^{3}He/^{4}He ($\times 10^{-7}$)	R/R_a	Ar ($\times 10^{-5}$)	^{40}Ar ($\times 10^{-5}$)	^{40}Ar* ($\times 10^{-5}$)	^{36}Ar ($\times 10^{-7}$)	^{40}Ar/^{36}Ar	^{38}Ar/^{36}Ar	C_1 (%)	$C_1/C_{1\text{-}5+}$	$\delta^{13}C$-C_1 (‰, PDB)
							(cc (STP)/ cc)						(cc (STP)/ cc)								
1	DF1-1S-5	DST	2002..9.16	Yinggehai	1802–1819.5	GATC	0.50	1.73	0.50	0.38	3.46	0.25	2.60	2.90	0.29	0.87	331.5	0.187	7.90	0.94	−37.1
2	DF1-1S-6		2002.9.16	Yinggehai	1559.8	GATC	0.30	1.27	0.30	0.21	4.23	0.31	460.00	473.21	11.20	154.74	305.8	0.186	8.85	0.84	−34.9
3					1786.7		0.40	2.78	0.40	0.20	6.94	0.50	370.00	367.93	−3.68	124.47	295.6	0.188	7.78	0.90	−31.8
4					1840.2		0.50	2.11	0.50	0.35	4.23	0.31	24.00	24.22	0.12	8.07	300.0	0.188	7.08	0.81	−31.3
5					2134.9		0.40	1.19	0.40	0.32	2.98	0.22	730.00	750.96	17.78	245.57	305.8	0.188	12.64	0.97	−36.7
6	DF1-1–11		2002.1.4	Huangliu	2785–2799	GATC	0.40	0.18	0.40	0.39	0.44	0.03	7.00	8.87	1.84	2.35	376.8	0.191	43.11	0.97	−30.1
7					3383–3403		0.70	0.79	0.70	0.65	1.13	0.08	110.00	107.68	−2.80	37.00	291.0	0.187	86.94	0.94	−30.3
8					3410–3450		0.50	0.45	0.50	0.47	0.90	0.06	18.00	18.15	0.08	6.06	299.8	0.187	78.40	0.85	−30.7
9	LD10-1–10		2020.10.16	Huangliu	4022.7–4062.5	ERC	0.69	0.35	0.69	0.67	0.51	0.04	8.47	8.78	0.27	2.85	308.0	0.188	/	/	/
10					4022.7–4062.5		0.96	0.47	0.96	0.94	0.49	0.04	5.20	5.52	0.30	1.75	315.6	0.186	/	/	/
11					4022.7–4062.5		0.54	0.54	0.54	0.50	1.01	0.07	13.99	14.54	0.49	4.71	308.9	0.190	/	/	/
12	LD10-3–1		2017.6.26	Meishan	4106–4151	ERC	2.61	2.03	2.61	2.49	0.78	0.06	1.03	1.83	0.80	0.35	528.0	0.183	67.66	0.97	−28.7
13	LD10-2–1		2019.6.13	Meishan	4101.5–4170.5	ERC	3.86	0.95	3.86	3.83	0.25	0.02	0.55	1.44	0.89	0.19	775.0	0.195	33.08	0.97	−28.2
14	DF1-1	Well head	2020.11.30	Yinggehai	/	GATC	0.44	0.13	0.44	0.43	0.30	0.02	1.00	1.52	0.52	0.34	452.0	0.173	/	/	/
15					/		0.61	0.15	0.61	0.61	0.24	0.02	0.90	2.02	1.12	0.30	668.0	0.182	/	/	/
16					/		0.74	2.86	0.74	0.54	3.87	0.28	422.40	440.50	16.26	142.10	310.0	0.189	/	/	/
17					/		0.99	0.13	0.99	0.99	0.13	0.01	2.20	7.25	5.04	0.74	979.0	0.186	/	/	/
18					/		0.83	0.15	0.83	0.83	0.18	0.01	1.10	3.99	2.88	0.37	1078.0	0.171	/	/	/
19					/		1.53	0.98	1.53	1.47	0.64	0.05	1.00	1.01	0.00	0.34	299.0	0.188	/	/	/
20					/		1.23	0.64	1.23	1.20	0.52	0.04	3.40	6.35	2.93	1.14	555.0	0.190	/	/	/
21					/		1.42	1.21	1.42	1.35	0.85	0.06	3.60	6.54	2.92	1.21	540.0	0.184	/	/	/
22					/		0.43	0.11	0.43	0.43	0.27	0.02	0.90	1.70	0.80	0.30	563.0	0.175	/	/	/
23					/		0.74	0.12	0.74	0.74	0.16	0.01	0.80	1.57	0.77	0.27	584.0	0.220	/	/	/
24					/		0.70	0.27	0.70	0.69	0.39	0.03	1.10	2.44	1.33	0.37	659.0	0.172	/	/	/
25	DF13-2		2020.11.30	Huangliu	/	GATC	1.20	0.12	1.20	1.20	0.10	0.01	0.70	2.09	1.38	0.24	886.0	0.220	/	/	/
26					/		1.17	0.20	1.17	1.17	0.17	0.01	2.10	6.75	4.64	0.71	955.0	0.218	/	/	/
27	LD22-1		2020.11.3	Ledong	/	GATC	1.58	0.37	1.58	1.57	0.24	0.02	3.30	11.22	7.91	1.11	1011.0	0.190	/	/	/
28					/		1.61	0.47	1.61	1.59	0.29	0.02	3.40	10.57	7.15	1.14	924.0	0.201	/	/	/
29					/		1.65	0.42	1.65	1.64	0.26	0.02	4.50	14.46	9.94	1.51	955.0	0.177	/	/	/
30					/		1.54	0.40	1.54	1.53	0.26	0.02	3.80	12.27	8.46	1.28	960.0	0.197	/	/	/
31					/		3.22	1.09	3.22	3.17	0.34	0.02	5.30	16.06	10.74	1.78	901.0	0.177	/	/	/
32	LD15-1		2020.11.3	Yinggehai	/	GATC	1.09	1.24	1.09	1.01	1.14	0.08	2.70	7.17	4.45	0.91	789.0	0.177	/	/	/
33					/		0.73	0.88	0.73	0.67	1.20	0.09	1.30	3.75	2.45	0.44	858.0	0.196	/	/	/
34					/		0.53	0.41	0.53	0.51	0.78	0.06	1.10	2.71	1.61	0.37	733.0	0.191	/	/	/
35					/		0.45	0.47	0.45	0.42	1.05	0.08	0.80	2.12	1.31	0.27	787.0	0.224	/	/	/
36					/		0.79	0.82	0.79	0.74	1.04	0.08	1.50	4.16	2.66	0.50	825.0	0.190	/	/	/
37					/		0.20	0.23	0.20	0.19	1.13	0.08	0.70	1.24	0.53	0.24	525.0	0.193	/	/	/
38					/		0.67	0.70	0.67	0.63	1.04	0.08	1.20	3.46	2.25	0.40	856.0	0.179	/	/	/
39					/		0.91	0.77	0.91	0.86	0.85	0.06	1.70	4.94	3.23	0.57	863.0	0.190	/	/	/
40					/		0.96	0.90	0.96	0.90	0.94	0.07	1.80	4.75	2.95	0.61	785.0	0.191	/	/	/
	Atmosphere						/	/	0.524	/	13.86	1.00	/	930	/	314.2	298.56	0.1885	/	/	/

DST: drill stem test; GATC: Geochemistry Analytical & Testing Center at the Northwest Institute of Eco-Environment and Resources (GATC) of the Chinese Academy of Sciences; ERC: Experimental Research Center (ERC) of the Wuxi Research Institute of Petroleum Geology, SINOPEC.
Concentrations are in cm^3 (STP)/cm^3, standard temperature and pressure are p = 0.101 MPa, T = 0 °C.
Atmosphere values are after Ballentine et al. (2002), Ozima and Podosek (2002), Mark et al. (2011), and Boucher et al. (2018).

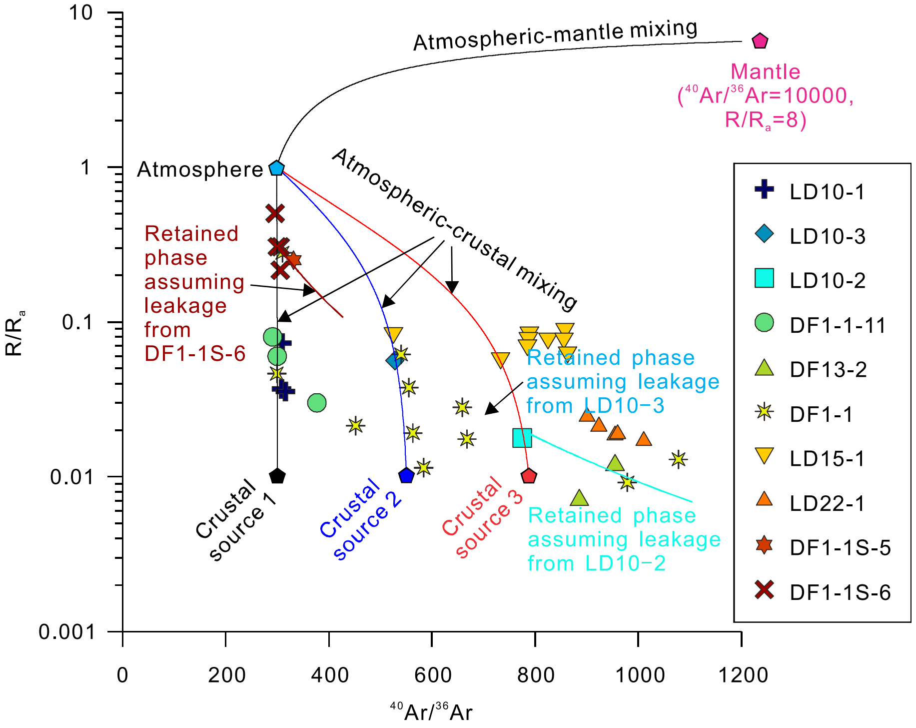

Fig. 3. Cross plot of ^{40}Ar/^{36}Ar with R/R_a. Leakage modeling results were established with Eq. (9). Atmospheric, crustal, and mantle values are after Ballentine et al. (2002), Graham (2002), and Ozima and Podosek (2002).

5. Discussion

5.1. Noble gas source

The measured R/R_a values of our samples are all much lower than the typical mantle value (e.g., the mid-ocean ridge basalts, MORB, have R/R_a = 8 (Ballentine et al., 2002; Graham, 2002), and also lower than the atmospheric value (R/R_a = 1). The minimum R/R_a value approaches the typical crustal value (R/R_a = 0.01, Ballentine and Burnard, 2002). Meanwhile, the measured ^{40}Ar/^{36}Ar ratios in the samples generally exceed the atmospheric value of 298.56 (Mark et al., 2011), but are significantly lower than the typical mantle value (>10,000, e.g., MORB has ^{40}Ar/^{36}Ar = 40,000) (Graham, 2002). These characteristics of R/R_a and ^{40}Ar/^{36}Ar suggest that the noble gases in the Yinggehai Basin samples primarily originate from a mixture of atmospheric and crustal sources (Fig. 3).

The volume proportion of crustal ^{4}He*, estimated by Eq. (1), ranges from 50% to 100%, which can be further divided into two groups: (1) DST samples from DF1-1S-5 and DF1-1S-6 that exhibit ^{4}He* proportions below 79% and (2) other samples showing ^{4}He* proportion of >90% (Fig. 6). The low ^{4}He* proportions exclude the dominant crustal ^{4}He* supply in DF1-1S-5 and DF1-1S-6. Similarly, the ^{40}Ar* proportion estimated by Eq. (2) varies from 0 to 70%, and can be classified into three groups: (1) samples from DF1-1S-5, DF1-1S-6, and LD10-1 wells generally exhibit ^{40}Ar* proportion below 20%; (2) most samples from LD10-3 field and some from DF1-1 field show slightly higher ^{40}Ar* proportion of 50%–60%; (3) the highest ^{40}Ar* proportions up to ~70% are observed in samples from LD10-2, LD22-1, LD15-1, and DF1-1 (Fig. 6). These observations suggest the presence of at least three distinct sources of crustal noble gases, with DF1-1S-6, LD10-3, and LD10-2 serving as representative samples of sources 1, 2, and 3, respectively (Fig. 6). Alternatively, if the crustal noble gases in the three groups originate from the same source, the observed variations in ^{4}He* and ^{40}Ar* proportions may reflect differences in their migration pathways. Additionally, the calculated ^{40}Ar*/^{4}He* ratios for these three groups also differ from one another, further supporting the hypothesis of three distinct crustal noble gas sources (Fig. 7).

Both the ^{40}Ar* proportion and ^{40}Ar/^{36}Ar value exhibit a consistent increasing trend across these three identified sources (Fig. 3). Considering that the release of ^{40}Ar* from solid minerals into pore fluids requires temperatures exceeding the closure temperature, this increasing trend in both ^{40}Ar* proportion and ^{40}Ar/^{36}Ar value indicates a progressively deeper, higher-temperature source of the crustal noble gases. The source with the highest ^{40}Ar/^{36}Ar ratio, referred as Source 3, is primarily associated with gas fields located near the suspected central fault, including the DF1-1 and DF13-2 fields in the northern Central depression and LD10-2, LD15-1, and LD22-1 fields in the southern Central depression (Figs. 1 and 6). In contrast, Source 1, with a lower ^{40}Ar/^{36}Ar ratio, appears to be more prevalent in gas fields further from the suspected central fault, e.g., DF1-1S-6, DF1-1S-5, and LD10-1 fields (Figs. 1 and 6). The observed spatial correlation between elevated ^{40}Ar/^{36}Ar values and the suspected central fault suggests that this fault may serve as a crucial conduit for the upward migration of high-temperature, crustal-derived noble gases into shallower layers.

5.2. Noble gas leakage

The Miocene to Pliocene sandstone reservoirs in the Yinggehai Basin have average Th, U, and K contents of approximately 12 ppm, 2.5 ppm, and 1.9 wt.%, respectively (Ma et al., 2017; Zheng et al., 2023). Assuming that Th and U in the reservoir rock have fully decayed to ^{4}He* and K has fully decayed to ^{40}Ar*, the predicted ^{40}Ar*/^{4}He* ratio from Eq. (7) is approximately 0.11 in

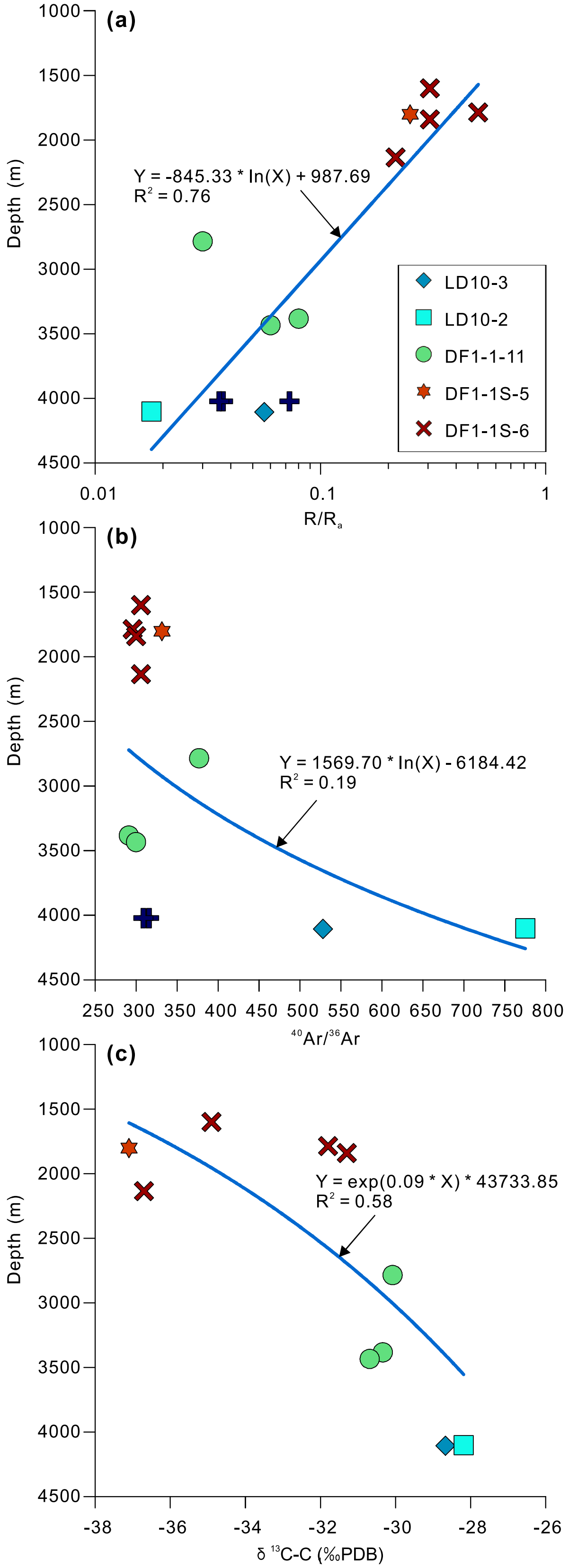

Fig. 4. Plots of R/R_a (a), $^{40}Ar/^{36}Ar$ (b), and carbon isotope of methane ($\delta^{13}C$-C_1) with burial depth for DST (drill stem test) samples.

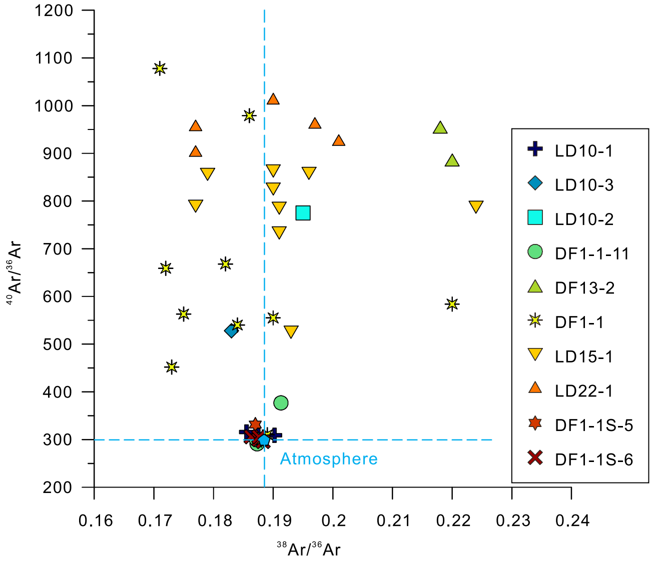

Fig. 5. Cross plot of $^{40}Ar/^{36}Ar$ with $^{38}Ar/^{36}Ar$. The atmosphere value is after Mark et al. (2011).

the gas reservoirs of the Yinggehai Basin. This prediction does not account for the effect of closure temperature on the release process. The current reservoir temperatures of the various gas fields in the Yinggehai Basin are higher than the closure temperature of $^4He^*$ (e.g., 50–70 °C in mica and feldspar), but lower than the $^{40}Ar^*$ closure temperature (e.g., 230–300 °C in mica and feldspar) (Liu et al., 2018; Jiang et al., 2022). The special temperature window may result in a lower release efficiency of $^{40}Ar^*$ relative to $^4He^*$ from minerals. Consequently, the $^{40}Ar^*/^4He^*$ ratio may be lower than the predicted value of 0.11.

However, the measured $^{40}Ar^*/^4He^*$ in the Yinggehai Basin gas fields ranges from 0.001 to 44.4. Notably, most samples show $^{40}Ar^*/^4He^*$ ratios above the predicted value of 0.11, as well as the average crustal value of 0.17–0.33 (Ballentine and Burnard, 2002), and the average mantle value of 0.25–0.67 (Graham, 2002; Fig. 7). Nevertheless, the measured $^{40}Ar^*/^4He^*$ ratios remain well below the atmosphere value of ~1770 (Ozima and Podosek, 2002; Fig. 7). The high $^{40}Ar^*/^4He^*$ ratios measured in some fields, such as LD10-2, LD10-3, and DF1-1S-5, align with the expected values from atmospheric-crustal binary mixing. In contrast, the measured $^{40}Ar^*/^4He^*$ ratios in other fields, e.g., LD15-1, LD22-1, and DF1-1, are much higher than the value predicted by atmospheric-crustal binary mixing (Fig. 7).

An abnormally high $^{40}Ar^*/^4He^*$ value indicates that the sample has experienced $^{40}Ar^*$ replenishment and/or $^4He^*$ depletion. Since the measured $^{40}Ar^*/^4He^*$ values exceed the average crustal value of 0.17–0.33 (Ballentine and Burnard, 2002), $^{40}Ar^*$ replenishment from deep crustal fluids (upper or lower crust) alone cannot fully account for the elevated value. A similar situation was reported by Zhou et al. (2005), who suggested that due to the lower solubility of $^4He^*$ in water as compared to $^{40}Ar^*$, $^4He^*$ is more easily exsolved into the gas phase from water phase and thus there is a $^{40}Ar^*/^4He^*$ increase in the water phase; once after massive gas loss, the gas newly exsolved from water also has an elevated $^{40}Ar^*/^4He^*$ ratio. Additionally, mass dependent fractionation can lead to preferential diffusive loss of lighter $^4He^*$ compared to the heavier $^{40}Ar^*$ during the leakage of the water-exsolved gas, which can further elevate the $^{40}Ar^*/^4He^*$ value of residual gas (Eqs. (9) and (10).

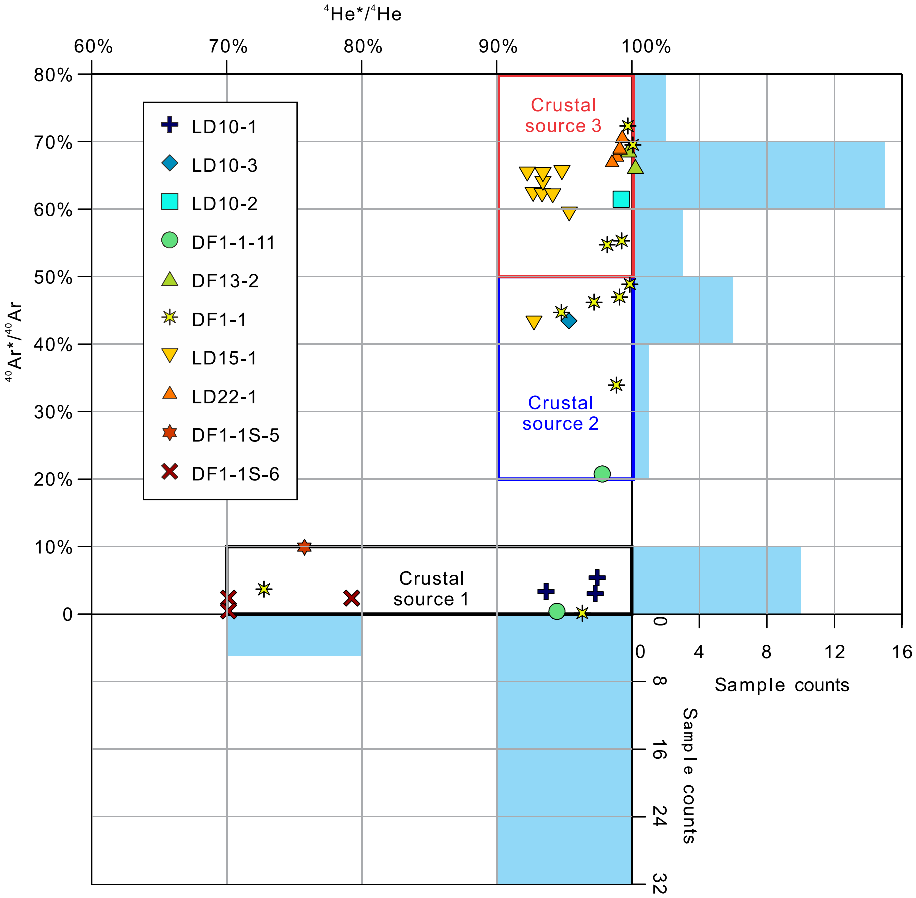

Fig. 6. Proportion of crustal ^{4}He* and ^{40}Ar*.

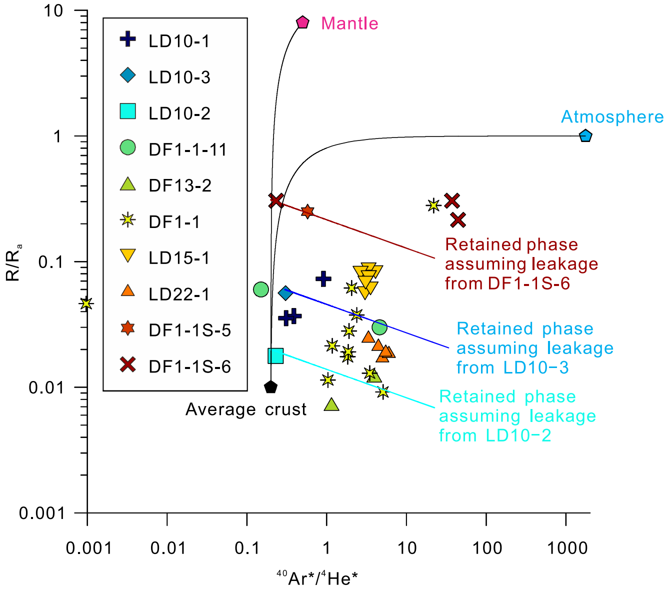

Fig. 7. Cross plot of ^{40}Ar*/^{4}He with R/R_a. Leakage modeling results were established with Eq. (9). Atmospheric, crustal, and mantle values are after Ballentine et al. (2002), Graham (2002), and Ozima and Podosek (2002).

Therefore, we suggest that the noble gas leakage is the key factor responsible for the abnormally high ^{40}Ar*/^{4}He* ratios (Fig. 8). This hypothesis is further supported by the modeling of solubility and mass dependent fractionations (Eqs. (9) and (10) using different initial noble gas sources (Fig. 9).

Samples exhibiting significant noble gas loss are primarily distributed within diapir structures, such as DF1-1-11, DF1-1, LD15-1, and LD22-1 (Figs. 1 and 10). This suggests that diapir activity may be a key mechanism triggering noble gas leakage, which compromises the integrity of gas traps. It is also noteworthy that some gas fields located farther from diapir structures but with a longer production history (~10 years) also show signs of noble gas loss (e.g., DF13-2) (Xie et al., 2014). Therefore, commercial natural gas extraction by human activities can be considered another potential mechanism for noble gas loss.

5.3. ^{4}He* age

As mentioned above, the concentrations of crustal noble gases (e.g., ^{4}He* and ^{40}Ar*) in a closed system primarily depend on the abundance of radioactive parent elements and the elapsed time since the system reached its closure temperatures (Eqs. (3)–(8). The closure temperature for ^{4}He* in clastic rock minerals is much lower than that for ^{40}Ar* (Ballentine et al., 1994; Snee, 2002). Thus, ^{4}He* accumulation time represents an earlier stage in the fluid system's history compared to ^{40}Ar*, making it a useful indicator for estimating the timing of fluid system closure.

The Miocene to Pliocene reservoirs in the Yinggehai Basin contains Th (12 ppm) and U (2.5 ppm) (Ma et al., 2017; Zheng et al., 2023). Assuming no external ^{4}He sources (i.e., ^{4}He$_{\text{extrernal}}$ = 0 in Eq. (4), the in-situ decay of Th and U would require 0.16–1130 Ma (^{4}He* accumulation ages) for the produced ^{4}He* reaching

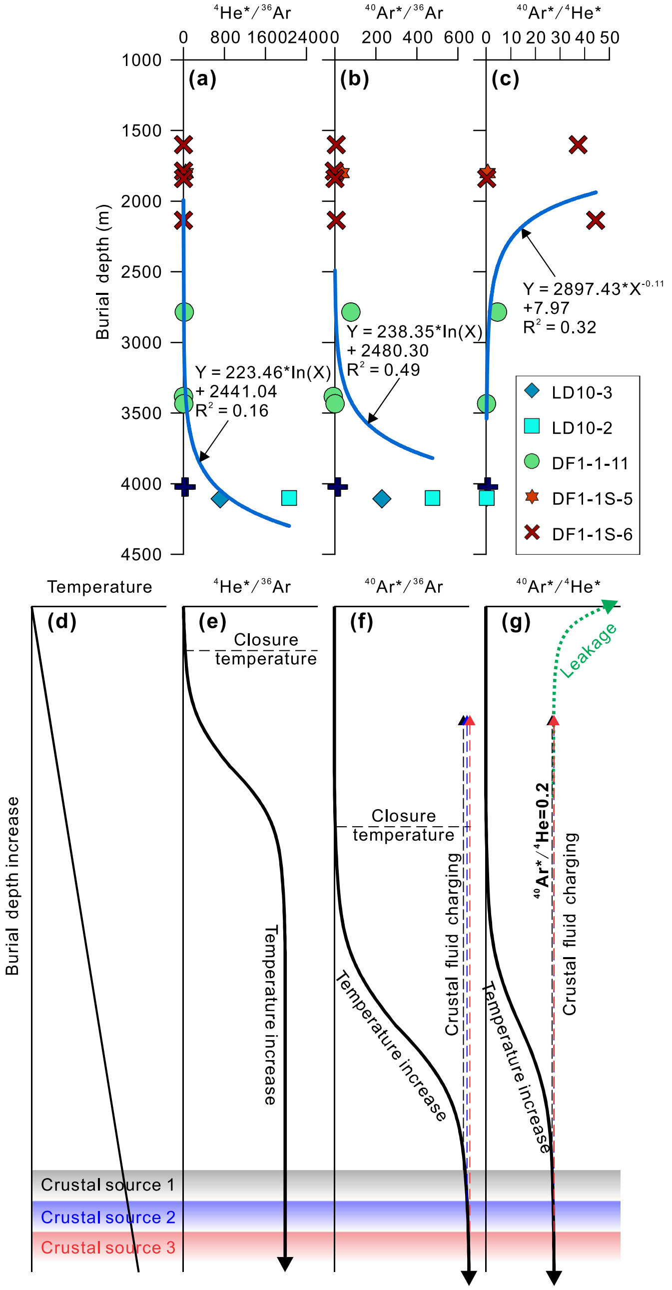

Fig. 8. Schematic diagram of ^{4}He*, ^{40}Ar*, and ^{40}Ar*/^{4}He* evolution (d–g) established from measured and calculated ^{4}He*/^{36}Ar (a), ^{40}Ar*/^{36}Ar (b), and ^{40}Ar*/^{4}He* (c) ratios.

calculated ^{4}He* concentrations, which significantly exceeds the deposition ages of most reservoirs (Table 2, Fig. 2). This discrepancy suggests that the $^4\mathrm{He}_{\mathrm{extrernal}}$ contribution cannot be ignored, consistent with the high-temperature noble gas source inferred from elevated ^{40}Ar/^{36}Ar value.

Given the shallow Moho depth (approximately 22–24 km) in the region (Fig. 1), it is likely that $^4\mathrm{He}_{\mathrm{extrernal}}$ originates from the deep crust (lower crust). Assuming a 10–11 km thickness for both upper and lower crust, the supply of deep crust $^4\mathrm{He}_{\mathrm{extrernal}}$ generally reduces the calculated ^{4}He* accumulation time, resulting in younger ages compared to deposition ages (Figs. 10 and 11a). Notably, noble gas leakage—particularly ^{4}He* depletion—was observed in some fields (Fig. 9). In cases of partial ^{4}He* loss, the measured ^{4}He* concentrations may underestimate the actual ^{4}He* accumulation age. Nevertheless, when the noble gas loss is minimal, ^{4}He* accumulation age remains a reliable proxy for estimating trap sealing time (Fig. 11b). Gas samples with insignificant noble gas leakage indicate three key ^{4}He* accumulation time windows: 4–4.5 Ma (e.g., LD10-2), 1–2 Ma (e.g., LD10-3), and 0–0.5 Ma (e.g., LD10-1) (Fig. 11c).

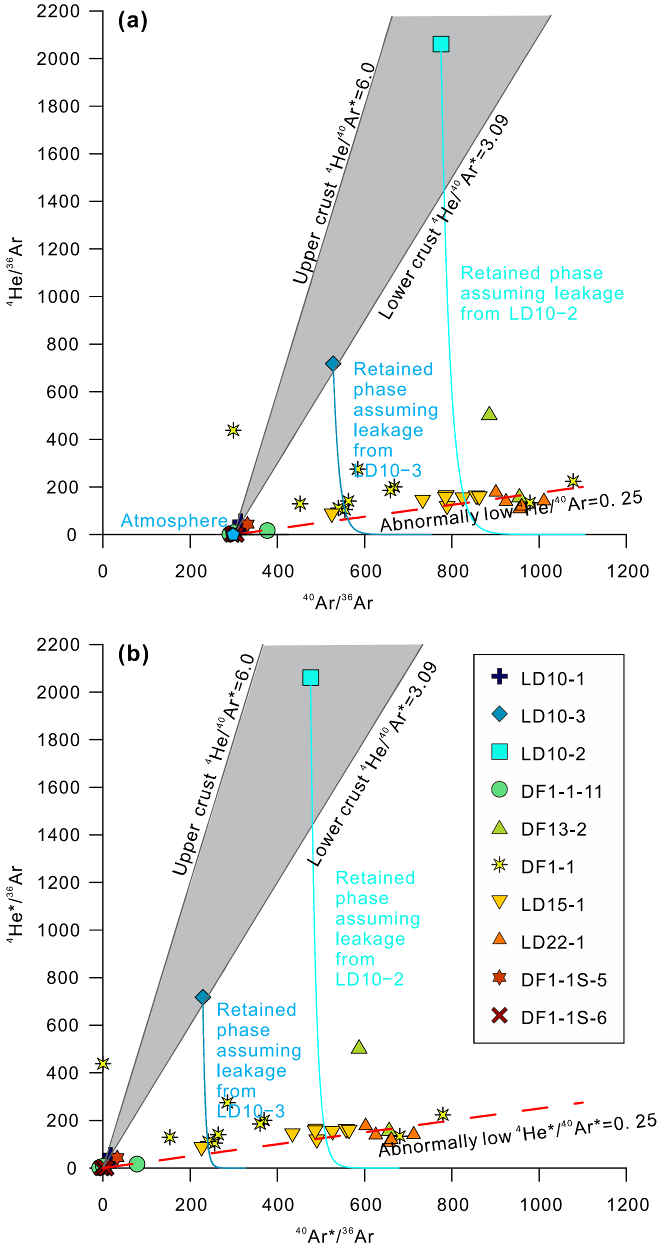

Fig. 9. Cross plots of (a) ^{4}He/^{36}Ar with ^{40}Ar/^{36}Ar and (b) ^{4}He*/^{36}Ar with ^{40}Ar*/^{36}Ar. Leakage modeling results were established with Eq. (9).

5.4. Implications for hydrocarbon source, migration, and accumulation

5.4.1. Sources of hydrocarbons

As mentioned above, the ^{40}Ar/^{36}Ar ratio of noble gases provides insights into the temperature of their source. Generally, higher ^{40}Ar/^{36}Ar values indicate that the noble gases originated from higher temperature environments (Fig. 4b). Additionally, the ^{40}Ar/^{36}Ar value positively correlates with the carbon isotope

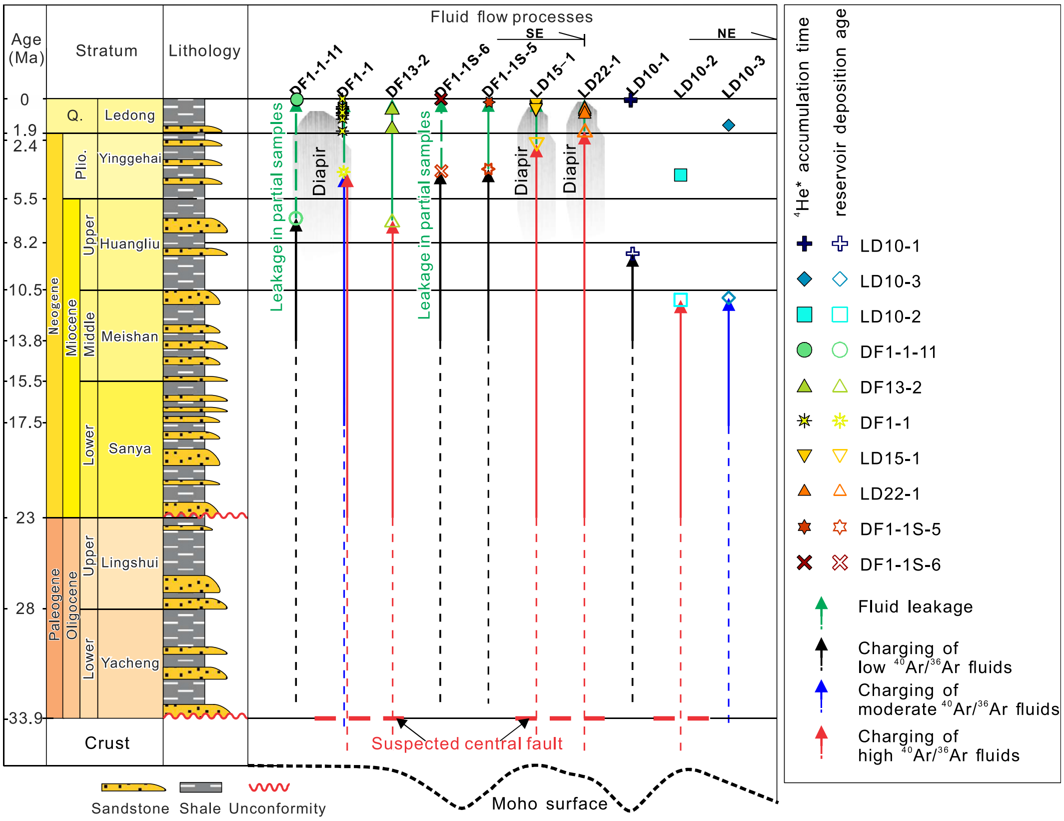

Fig. 10. Schematic diagram of noble gas flow in the sedimentary stratigraphic framework of the Yinggehai Basin.

of methane (δ^{13}C-C$_1$) and the dryness ratio (C$_1$/C$_{1\text{-}5}$) (Fig. 12). Both δ^{13}C-C$_1$ and C$_1$/C$_{1\text{-}5}$ of hydrocarbon gas positively relate to thermal maturity (Prinzhofer and Huc, 1995). Therefore, elevated ^{40}Ar/^{36}Ar values suggest the existence of fluid migration pathways that transport deeply sourced, highly mature hydrocarbons from depth to shallower layers (Fig. 4c). These migration pathways, likely associated with the suspected central fault, facilitate the movement of high-temperature crustal fluids and hydrocarbons.

Hydrocarbons in the Yinggehai Basin likely originated from two primary source rocks: the Lower Miocene Sanya Formation and the Middle Miocene Meishan Formation (Liu et al., 2024). Due to its older age and deeper burial, the Lower Miocene Sanya Formation generated hydrocarbons earlier at higher thermal maturity than the Middle Miocene Meishan Formation. As a result, the deep-buried reservoirs of LD10-2 field, which are located closer to the suspected central fault, contain more highly matured hydrocarbons generated by the Lower Miocene Sanya Formation as compared to the shallower reservoirs of LD10-3, which is farther from the fault (Fig. 12).

5.4.2. Mechanisms of hydrocarbon migration

Because of the similar solubility of methane (C$_1$) and ^{36}Ar in water, the C$_1$/^{36}Ar ratio in gas phase exsolved from water should be similar to the initial C$_1$/^{36}Ar ratio in the water phase (Ballentine et al., 1991, 2002). The C$_1$/^{36}Ar ratio in water is a function of temperature, pressure, and brine salinity (Ballentine et al., 2002). Using the average geothermal gradient of ~ 42 °C/km (He et al., 2002; Zheng et al., 2023) and a water salinity of 5 M NaCl, the predicated C$_1$/^{36}Ar ratios in the Yinggehai Basin reservoirs are shown in Fig. 13. The measured C$_1$/^{36}Ar ratios in most samples, particularly those from fields with insignificant noble gas leakage (e.g., LD10-2 and LD10-3), are much higher than the predicated C$_1$/^{36}Ar ratios. This indicates that methane in these samples likely primarily migrated and accumulated in the gas phase, rather than being exsolved from water. In contrast, a subset of samples from gas fields exhibiting noble gas loss (e.g., some samples from DF1-1S-6) have measured C$_1$/^{36}Ar values that closely match the predicted values, suggesting that, in these cases, methane may have migrated as a dissolved phase in formation water before exsolving into the gas phase. Similar water-dissolved methane was also reported by Xie and Huang (2014).

5.4.3. Stages of hydrocarbon accumulation

Fluid inclusion analyses of Upper Miocene to Pliocene reservoirs in the Yinggehai Basin indicate that hydrocarbon charging primarily occurred within the past ~5 Ma. For instance, the reservoirs of the LD10-1, LD10-2, and LD10-3 fields were charged with hydrocarbons at 4.0–2.9 Ma, 2.0–1.2 Ma, and 0.8–0.3 Ma, respectively (Jiang et al., 2022). Similarly, previous research suggested that the DF1-1 field experienced three distinct episodes of hydrocarbon charging at 3.7 Ma, 1.8 Ma, and 0.4 Ma (Xie et al., 2012). These hydrocarbon charging periods align very well with the ^{4}He* accumulation time windows (Fig. 11b and c), suggesting that hydrocarbons were effectively preserved and sealed after charging.

In summary, spatial heterogeneity in hydrocarbon accumulation is primarily controlled by two factors: (1) fluid migration pathways and (2) the timing of trap sealing. Proximity to the suspected central fault systems, which severed as the primary conduits, governed the fluid sources of various thermal maturities. For instance, the LD10-2 field is more closely connected to the suspected central fault than the LD10-1 and LD10-3 fields, resulting in predominant sourcing from deeper, higher-maturity fluids which

Table 2
^{4}He* accumulation time of gas field in the Yinggehai Basin.

No.	Fields (or wells)	$^4He^*_{water}$ ($\times 10^{-4}$) (cc (STP)/g_{water})	ρ_{rock} (g/cm^3)	ω (%)	$P(^4He^*)_{in\text{-}situ}$ ($\times 10^{-13}$) (cc (STP)/g_{rock}/year)	$^4He^*_{in\text{-}situ}$ ($\times 10^{-12}$) (cc (STP)/year)	$t_{in\text{-}situ}$ (Ma)	$\rho_{upper\ crust}$ (g/cm^3)	$H_{upper\ crust}$ (m)	$P(^4He^*)_{upper\ crust}$ ($\times 10^{-13}$) (cc (STP)/g_{rock}/year)	$\rho_{lower\ crust}$ (g/cm^3)	$H_{lower\ crust}$ (m)	$P(^4He^*)_{lower\ crust}$ ($\times 10^{-14}$) (cc (STP)/g_{rock}/year)	h (m)	$^4He^*_{external}$ ($\times 10^{-9}$) (cc (STP)/year)	$t_{in\text{-}situ+external}$ (Ma)
1	DF1-1S-5	3.31	2.4	20.0	6.46	6.20	53.44	2.60	10,000	6.45	3.30	10,000	6.42	50.00	1.89	0.175
2	DF1-1S-6	0.01		20.0		6.20	0.17								1.89	0.001
3		0.01					0.20									0.001
4		0.33					5.36									0.018
5		0.01					0.16									0.001
6	DF1-1–11	1.27		15.0		8.78	14.47								2.52	0.050
7		0.13					1.53									0.005
8		0.60					6.79									0.024
9	LD10-1–10	1.81		10.0		13.95	12.95								3.78	0.048
10		4.11					29.44									0.108
11		0.82					5.85									0.022
12	LD10-3–1	54.92		10.0		13.95	393.71								3.78	1.449
13	LD10-2–1	157.68		10.0		13.95	1130.37								3.78	4.159
14	DF1-1	9.89		20		6.20	147.27								1.89	0.522
15		15.30					227.76									0.808
16		0.03					0.43									0.002
17		10.24					152.49									0.541
18		17.11					254.73									0.903
19		33.52					499.05									1.769
20		8.00					119.07									0.422
21		8.50					126.59									0.449
22		10.76					160.28									0.568
23		21.01					312.75									1.109
24		14.21					211.54									0.750
25	DF13-2	39.09		15		8.78	410.82								2.52	1.547
26		12.64					132.84									0.500
27	LD22-1	10.81		20		6.20	174.37								1.89	0.571
28		10.65					171.75									0.562
29		8.27					133.34									0.436
30		9.13					147.31									0.482
31		13.61					219.59									0.718
32	LD15-1	8.51		20		6.20	137.26								1.89	0.449
33		11.78					190.02									0.622
34		10.45					168.52									0.552
35		11.94					192.60									0.630
36		11.19					180.48									0.591
37		6.03					97.22									0.318
38		11.86					191.33									0.626
39		11.54					186.20									0.609
40		11.42					184.17									0.603

Reservoir porosities of Ledong-Yingeghai, Huangliu, and Meishan Formations are after Wang and Huang (2008), Zhang et al. (2013), and Fan et al. (2021), respectively.
The density and ^{4}He* generation rate of the Upper and Lower crust are after Zhou and Ballentine (2006) and Wen et al. (2015).

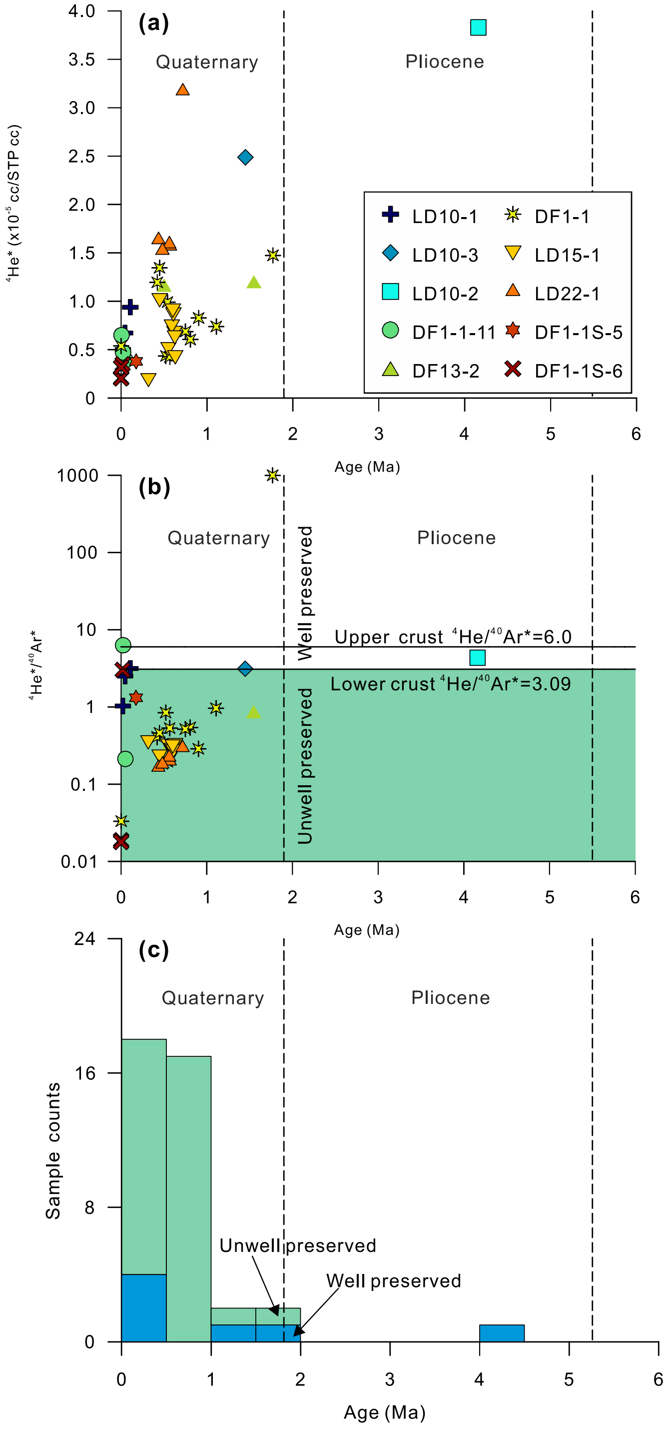

Fig. 11. Cross plots of accumulation time (age) with (a) ^{4}He* concentration (b) ^{4}He*/^{40}Ar* ratio, and (c) sample counts.

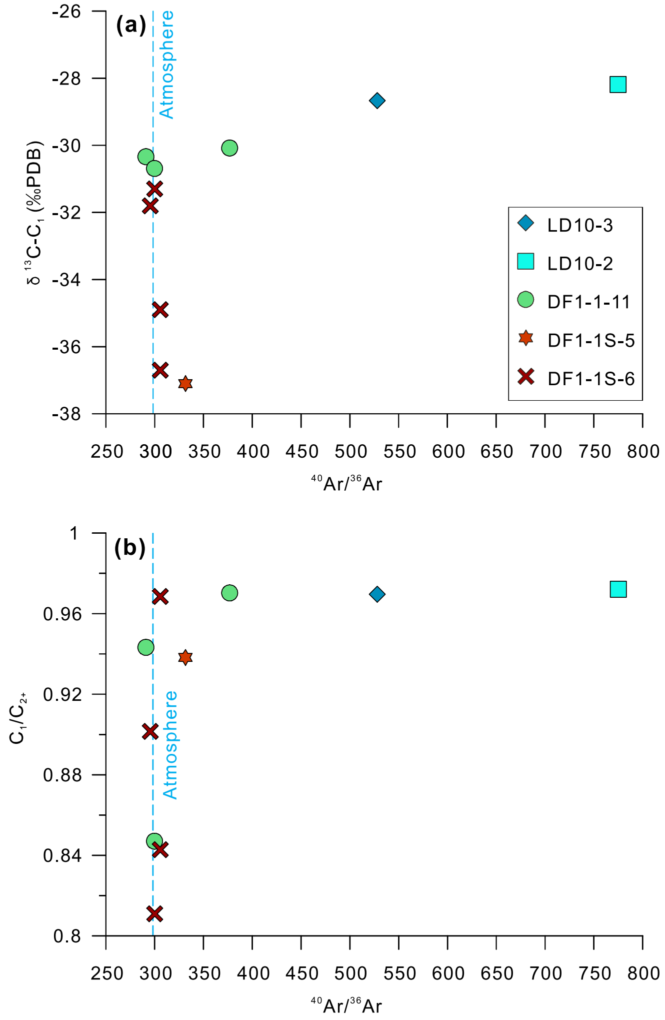

Fig. 12. Cross plots of (a) δ^{13}C-C$_1$ value and (b) dryness ratio ($C_1/C_{1\text{-}5}$) with ^{40}Ar/^{36}Ar ratio.

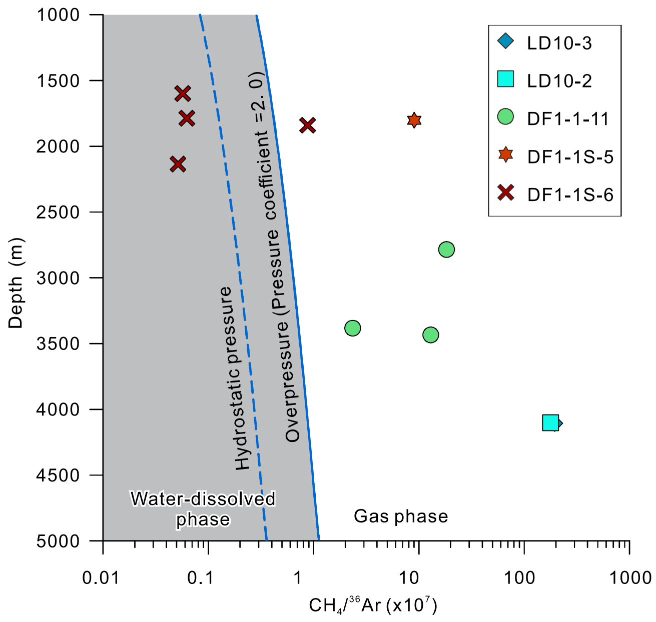

Fig. 13. Predicted and measured values of C$_1$/^{36}Ar in the Yinggehai Basin.

were characterized by elevated ^{40}Ar/^{36}Ar ratios (Fig. 14a and b). Although deep-to-shallow fluid migration may occur episodically in multiple time windows, the thermal maturity of accumulated hydrocarbons is dominantly regulated by the trap sealing chronology (Fig. 14a and b). As shown in Fig. 14c, during the Early Pliocene, multiple fault systems facilitated migration of high-maturity hydrocarbons (high $C_1/C_{1\text{-}5}$ ratios and enriched δ^{13}C-C$_1$) from the Lower Miocene Sanya Formation into all three LD10-1, LD10-2, and LD10-3 traps; however, only the LD10-2 trap achieved effec-

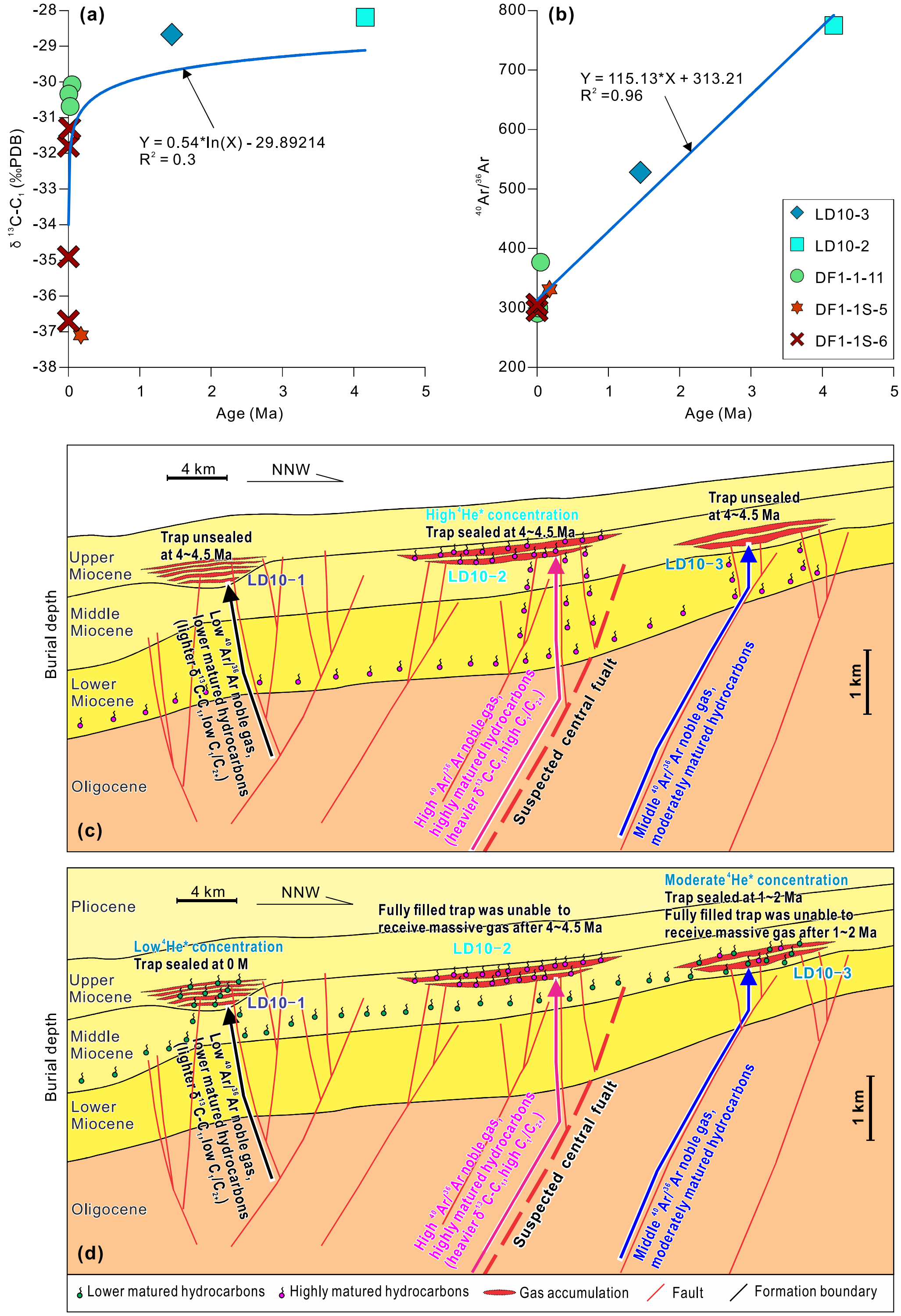

Fig. 14. Correlations of trap sealing time (age) with (a) δ^{13}C-C$_1$ value and (b) ^{40}Ar/^{36}Ar ratio. Hydrocarbon accumulation model during the (c) Early Pliocene and (d) Quaternary, revealed by noble gas geochemical characteristics in the Yinggehai Basin. The framework of faults and formations is adapted from Jiang et al. (2022).

tive sealing at 4–4.5 Ma, which preserved the Sanya-sourced hydrocarbons. In contrast, the LD10-1 and LD10-3 traps remained unsealed, resulting in the bypass of highly mature hydrocarbons of the Sanya Formation (Fig. 14c). Subsequently, massive hydrocarbons generated by the Meishan Formation migrated into the LD10-1, 10–2, and LD10-3 traps during the Quaternary. At this stage, the LD10-2 trap, which was already fully filled with earlier Sanya-derived hydrocarbons, reached its spill point, preventing the retention of Meishan-derived hydrocarbons. Conversely, the LD10-3 and LD10-1 traps, having remained underfilled and received Meishan-sourced hydrocarbons at 1–2 Ma and ~0 Ma, respectively (Fig. 14d).

6. Conclusion

Noble gas geochemical analyses from 10 gas fields in the Yinggehai Basin reveal significant spatial and temporal heterogeneity in fluid activities and hydrocarbon accumulation. The measured $^3He/^4He$ values range from the average crustal value to the atmospheric value, while the $^{40}Ar/^{36}Ar$ values exceed atmospheric levels, indicating the binary mixing of atmospheric-derived and crustal-derived noble gases. More than 70% of ^4He and 0–72% of ^{40}Ar are estimated to originate from the crust. Spatially, proximity to the suspected central fault correlates with higher-temperature crustal fluids, as evidenced by greater $^{40}Ar^*$ proportions and higher $^{40}Ar/^{36}Ar$ values. The $^{40}Ar^*/^4He^*$ ratios generally follow the expected binary mixing trend of atmospheric and crustal sources in well-preserved gas fields. However, noble gas fractionation caused by both natural (diapir activity) and artificial (long-term production) leakage can lead to abnormally high $^{40}Ar^*/^4He^*$ ratios. The estimated $^4He^*$ accumulation times indicate three key gas preservation windows: 4–4.5 Ma, 1–2 Ma, and 0–0.5 Ma. The suspected central fault not only served as a migration conduit for high-temperature crustal fluids with elevated $^{40}Ar/^{36}Ar$ values but also facilitated the transport of deep-seated, highly mature hydrocarbons characterized by high $\delta^{13}C_1$ and $C_1/C_{1\text{-}5}$ ratios.

Most samples exhibit high $C_1/^{36}Ar$ values, indicating that C_1 primarily migrated in the gas phase rather than as a dissolved component in water. However, some shallow gas fields show lower $C_1/^{36}Ar$ values after gas leakage, suggesting that methane migration in these cases may have involved water dissolution. The timing of trap sealing and the depth of migration pathways played critical roles in hydrocarbon accumulation. Early trap sealing and deep migration pathways favored the accumulation of hydrocarbons generated by the Lower Miocene Sanya Formation. In contrast, later trap sealing and shallower migration depths were more conducive to the accumulation of hydrocarbons sourced from the Middle Miocene Meishan Formation.

CRediT authorship contribution statement

Rui Liu: Writing – review & editing, Writing – original draft, Investigation, Formal analysis, Data curation, Conceptualization. **Rui Xu:** Writing – original draft, Investigation, Formal analysis. **Tao Wen:** Writing – review & editing, Writing – original draft, Methodology, Investigation, Conceptualization. **Khi Atchinson:** Writing – review & editing, Validation, Investigation. **Ziqi Feng:** Investigation, Visualization, Writing – review & editing. **Fang Hao:** Writing – review & editing, Visualization, Resources, Project administration. **Lin Hu:** Validation, Resources, Investigation, Data curation. **Jinqiang Tian:** Writing – review & editing, Visualization. **Yazhen Zhang:** Validation, Investigation, Data curation. **Jianzhang Liu:** Validation, Investigation. **Lei Tuo:** Validation, Formal analysis, Data curation.

Declaration of competing interest

The authors declare that they have no known competing financial interests or personal relationships that could have appeared to influence the work reported in this paper.

Acknowledgements

This study was supported by National Science and Technology Major Project for Deep Earth (No. SQ2025AAA060128), CNOOC Ltd. (KJZH-2021-0003-00), and the Science and Technology Innovation Program of Laoshan Laboratory (No. LSKJ202203403). We appreciate the collaboration and enthusiastic support of Lixia Shen, Yangyu Wu, and Lei Shao at the Hainan Branch of CNOOC Ltd.

References

Ballentine, C.J., Burgess, R., Marty, B., 2002. Tracing fluid origin, transport and interaction in the crust. Rev. Mineral. Geochem. 47, 539–614.

Ballentine, C.J., Burnard, P.G., 2002. Production, release and transport of noble gases in the continental crust. Rev. Mineral. Geochem. 47, 481–538.

Ballentine, C.J., Mazurek, M., Gautschi, A., 1994. Thermal constraints on crustal rare gas release and migration: Evidence from Alpine fluid inclusions. Geochim. Cosmochim. Acta 58, 4333–4348.

Ballentine, C.J., O'Nions, R.K., Oxburgh, E.R., Horvath, F., Deak, J., 1991. Rare gas constraints on hydrocarbon accumulation, crustal degassing and groundwater flow in the Pannonian Basin. Earth Planet. Sci. Lett. 105, 229–246.

Barry, P.H., Lawson, M., Meurer, W.P., Danabalan, D., Byrne, D.J., Mabry, J.C., Ballentine, C.J., 2017. Determining fluid migration and isolation times in multiphase crustal domains using noble gases. Geology 45, 775–778.

Barry, P.H., Lawson, M., Meurer, W.P., Warr, O., Mabry, J.C., Byrne, D.J., Ballentine, C. J., 2016. Noble gases solubility models of hydrocarbon charge mechanism in the Sleipner Vest gas field. Geochim. Cosmochim. Acta 194, 291–309.

Battani, A., Sarda, P., Prinzhofer, A., 2000. Basin scale natural gas source, migration and trapping traced by noble gases and major elements: the Pakistan Indus basin. Earth Planet. Sci. Lett. 181, 229–249.

Bauer, S.J., Gardner, W.P., Lee, H., 2016. Release of radiogenic noble gases as a new signal of rock deformation. Geophys. Res. Lett. 43, 10688–10694.

Boucher, C., Lan, T., Mabry, J., Bekaert, D.V., Burnard, P.G., Marty, B., 2018. Spatial analysis of the atmospheric helium isotopic composition: Geochemical and environmental implications. Geochim. Cosmochim. Acta 237, 120–130.

Brown, A., 2019. Origin of helium and nitrogen in the Panhandle-Hugoton field of Texas, Oklahoma, and Kansas, United States. AAPG Bull. 103, 369–403.

Byrne, D.J., Barry, P.H., Lawson, M., Ballentine, C.J., 2018. Noble gases in conventional and unconventional petroleum systems. Geol. Soc. Lond. Spec. Publ. 468, 127–149.

Byrne, D.J., Barry, P.H., Lawson, M., Ballentine, C.J., 2020. The use of noble gas isotopes to constrain subsurface fluid flow and hydrocarbon migration in the East Texas Basin. Geochim. Cosmochim. Acta 268, 186–208.

Chen, B., Liu, Y., Fang, L., Xu, S., Stuart, F.M., Liu, C., 2023. A review of noble gas geochemistry in natural gas from sedimentary basins in China. J. Asian Earth Sci. 246, 105578.

Chen, C., Qin, S., Wang, Y., Holland, G., Wynn, P., Zhong, W., Zhou, Z., 2022. High temperature methane emissions from Large Igneous Provinces as contributors to late Permian mass extinctions. Nat. Commun. 13, 6893.

Chen, Z., Liu, R., Tian, J., Hao, F., Hu, L., Hu, G., Zhang, Y., 2025. Influence of overpressured fluid expulsion on hydrocarbon accumulation in deep-buried Miocene reservoirs of the Yinggehai Basin, Northwestern South China Sea. Terra Nova 37, 129–140.

Clift, P.D., Sun, Z., 2006. The sedimentary and tectonic evolution of the Yinggehai–Song Hong basin and the southern Hainan margin, South China Sea: Implications for Tibetan uplift and monsoon intensification. J. Geophys. Res. Solid Earth 111, B06405.

Dang, Y.Y., 2023. Seismic sedimentology of submarine fan system in the 1st Member of the Huangliu Formation, Dongfang area, Yinggehai Basin, China. Bulletin of Geological Science and Technology 42 (6), 118–128 (in Chinese with English abstract).

Fan, C., Cao, J., Luo, J., Li, S., Wu, S., Dai, L., Hou, J., Mao, Q., 2021. Heterogeneity and influencing factors of marine gravity flow tight sandstone under abnormally high pressure: A case study from the Miocene Huangliu Formation reservoirs in LD10 area, Yinggehai Basin, South China Sea. Petrol. Explor. Dev. 48, 1048–1062.

Gao, Y., Qu, H., Chen, S., Zhou, W., Mo, F., 2021. Genetic characteristics of wave-dominated delta: A case study on Pliocene Ying Ⅱ Member in the Dongfang 1-1 gas field, Yinggehai Basin. Marine Geology Frontiers 37, 42–52 (in Chinese with English abstract).

Gilfillan, S.M.V., Ballentine, C.J., Holland, G., Blagburn, D., Lollar, B.S., Stevens, S., Schoell, M., Cassidy, M., 2008. The noble gas geochemistry of natural CO_2 gas reservoirs from the Colorado Plateau and Rocky Mountain provinces, USA. Geochim. Cosmochim. Acta 72 (4), 1174–1198.

Gong, Z.S., Li, S.T., 1997. Continental Margin Basin Analysis and Hydrocarbon Accumulation of the Northern South China Sea. Science Press, Beijing (in Chinese).

Graham, D.W., 2002. Noble gas isotope geochemistry of mid-ocean ridge and ocean island basalts: Characterization of mantle source reservoirs. Rev. Mineral. Geochem. 47, 247–317.

Han, G., Pinti, D.L., Castro, M.C., Hernández-Hernández, M.A., Lopez-Hernández, A., Hall, C.M., Zheng, G., Ramírez-Montes, M., 2022. Heat, noble gases and CO_2 sources in geothermal fields of Mexico. Appl. Geochem. 144, 105391.

He, L., Xiong, L., Wang, J., 2002. Heat flow and thermal modeling of the Yinggehai Basin, South China Sea. Tectonophysics 351, 245–253.

Horiguchi, K., Matsuda, J.I., 2013. Geographical distribution of $^3He/^4He$ ratios in north Kyushu, Japan: Geophysical implications for the occurrence of mantle-derived fluids at deep crustal levels. Chem. Geol. 340, 13–20.

Huang, B., Tian, H., Huang, H., Yang, J., Xiao, X., Li, L., 2015. Origin and accumulation of CO_2 and its natural displacement of oils in the continental margin basins, northern South China Sea. AAPG Bull. 99, 1349–1369.

Huang, B.J., Xiao, X.M., Hu, Z.L., Yi, P., 2005. Geochemistry and episodic accumulation of natural gases from the Ledong gas field in the Yinggehai Basin, offshore South China Sea. Org. Geochem. 36, 1689–1702.

Hunt, A.G., Darrah, T.H., Poreda, R.J., 2012. Determining the source and genetic fingerprint of natural gases using noble gas geochemistry: A northern Appalachian Basin case study. AAPG Bull. 96, 1785–1811.

Jiang, P., He, S., Yang, Z., Yang, K., Wang, M., Lan, Z., Ren, S., Zhang, R., Zhao, X., Yao, G., 2022. High CO_2 natural gas charging events, timing and accumulation pattern in LD10 area of Yinggehai Basin. Earth Sci. 47, 1569–1585 (in Chinese with English abstract).

Karolytė, R., Barry, P.H., Hunt, A.G., Kulongoski, J.T., Tyne, R.L., Davis, T.A., Wright, M. T., McMahon, P.B., Ballentine, C.J., 2021. Noble gas signatures constrain oil-field water as the carrier phase of hydrocarbons occurring in shallow aquifers in the San Joaquin Basin, USA. Chem. Geol. 584, 120491.

Kennedy, B.M., van Soest, M.C., 2007. Flow of mantle fluids through the ductile lower crust: Helium isotope trends. Science 318 (5855), 1433–1436.

Li, Y., Cao, C., Hu, H., Huang, H., 2022. The use of noble gases to constrain subsurface fluid dynamics in the hydrocarbon systems. Front. Earth Sci. 10, 895312. https://doi.org/10.3389/feart.2022.895312.

Li, Y., Qin, S., Wang, Y., Holland, G., Zhou, Z., 2020. Tracing interaction between hydrocarbon and groundwater systems with isotope signatures preserved in the Anyue gas field, central Sichuan Basin, China. Geochim. Cosmochim. Acta 274, 261–285.

Lin, J., Liu, R., Heinemann, N., Miocic, J.M., Tian, J., Chen, Z., Hu, L., Zhang, Y., Amalberti, J., Wang, L., 2024. CO_2 retention in high-pressure/high-temperature reservoirs of the Yinggehai Basin, northwestern South China Sea. Int. J. Greenh. Gas Con. 138, 104237.

Liu, H., Guo, X., Tuo, L., Wu, Y., Li, S., Xia, L., 2024. Organic facies characteristics of Miocene marine source rocks in Yinggehai Basin. Marine Geology Frontiers 40, 28–35 (in Chinese with English abstract).

Liu, R., Hao, F., Zhu, W., Liu, J., Xie, Y., Wang, Z., Wang, L., 2018. Variation of system openness and geochemical features in overpressured sandstones of the Yinggehai Basin, offshore South China Sea. Mar. Petrol. Geol. 92, 179–192.

Liu, R., Heinemann, N., Liu, J., Zhu, W., Wilkinson, M., Xie, Y., Wang, Z., Wen, T., Hao, F., Haszeldine, R.S., 2019. CO_2 sequestration by mineral trapping in natural analogues in the Yinggehai Basin, South China Sea. Mar. Petrol. Geol. 104, 190–199.

Liu, R., Wen, T., Amalberti, J., Zheng, J., Hao, F., Jiang, D., 2021. The dichotomy in noble gas signatures linked to tectonic deformation in Wufeng-Longmaxi Shale, Sichuan Basin. Chem. Geol. 581, 120412.

Liu, R., Wen, T., Pinti, D.L., Xu, R., Hao, F., Xu, S., Shu, Z., 2025. Noble gases in Paleozoic shale fluids document tectonic events and fluid migration in the Upper Yangtze Block. Int. J. Coal Geol. 297, 104671.

Ma, L., Castro, M.C., Hall, C.M., 2009. Crustal noble gases in deep brines as natural tracers of vertical transport processes in the Michigan Basin. Geochem. Geophys. Geosyst. 10, Q06001.

Ma, M., Li, C., Lv, C., Chen, G., Yang, F., Yan, Y., Yin, N., Zhang, G., 2017. Geochemistry and provenance of a multiple-stage fan in the Upper Miocene to the Pliocene in the Yinggehai and Qiongdongnan basins, offshore South China Sea. Mar. Petrol. Geol. 79, 64–80.

Mark, D.F., Stuart, F.M., de Podesta, M., 2011. New high-precision measurements of the isotopic composition of atmospheric argon. Geochim. Cosmochim. Acta 75, 7494–7501.

National Research Council, 2010. Selling the Nation's Helium Reserve. The National Academies Press, Washington, D.C., 156 p. https://doi.org/10.17226/12844.

Ozima, M., Podosek, F.A., 2002. Noble Gas Geochemistry. Cambridge University Press, New York.

Prinzhofer, A.A., Huc, A.Y., 1995. Genetic and post-genetic molecular and isotopic fractionations in natural gases. Chem. Geol. 126, 281–290.

Pinti, D.L., Castro, M.C., Shouakar-Stash, O., Tremblay, A., Garduño, V.H., Hall, C.M., Hélie, J.F., Ghaleb, B., 2013. Evolution of the geothermal fluids at Los Azufres, Mexico, as traced by noble gas isotopes, $\delta^{18}O$, δD, $\delta^{13}C$ and $^{87}Sr/^{86}Sr$. J. Volcanol. Geoth. Res. 249, 1–11.

Snee, L.W., 2002. Argon thermochronology of mineral deposits; a review of analytical methods, formulations, and selected applications. USGS Publication, p. 39. https://pubs.usgs.gov/publication/b2194.

Sun, Z., Zhou, D., Zhong, Z.H., Zeng, Z.X., Wu, S.M., 2003. Experimental evidence for the dynamics of the formation of the Yinggehai basin, NW South China Sea. Tectonophysics 372, 41–58.

Tolstikhin, I.N., Ballentine, C.J., Polyak, B.G., Prasolov, E.M., Kikvadze, O.E., 2017. The noble gas isotope record of hydrocarbon field formation time scales. Chem. Geol. 471, 141–152.

Wang, Z., Huang, B., 2008. Dongfang 1-1 gas field in the mud diapir belt of the Yinggehai Basin, South China Sea. Mar. Pet. Geol. 25, 445–455.

Wen, T., Castro, M.C., Ellis, B.R., Hall, C.M., Lohmann, K.C., 2015. Assessing compositional variability and migration of natural gas in the Antrim Shale in the Michigan Basin using noble gas geochemistry. Chem. Geol. 417, 356–370.

Wen, T., Castro, M.C., Nicot, J.-P., Hall, C.M., Larson, T., Mickler, P., Darvari, R., 2016. Methane sources and migration mechanisms in shallow groundwaters in Parker and Hood counties, Texas—A heavy noble gas analysis. Environ. Sci. Technol. 50, 12012–12021.

Wen, T., Castro, M.C., Nicot, J.-P., Hall, C.M., Pinti, D.L., Mickler, P., Darvari, R., Larson, T., 2017. Characterizing the noble gas isotopic composition of the Barnett Shale and Strawn Group and constraining the source of stray gas in the Trinity aquifer, North-Central Texas. Environ. Sci. Technol. 51, 6533–6541.

Xie, Y., 2019. Quantitative evaluation of sealing capacity of high temperature and pressure caprocks in Yinggehai Basin. Earth Sci. 44, 2579–2589 (in Chinese with English abstract).

Xie, Y., Huang, B., 2014. Characteristics and accumulation mechanisms of the Dongfang 13-1 hightemperature and overpressured gas field in the Yinggehai Basin, the South China Sea. Sci. China Earth Sci. 57, 2799–2807. https://doi.org/10.1007/s11430-014-4934-0.

Xie, Y., Zhang, Y., Li, X., Zhu, J., Tong, C., 2012. Main controlling factors and formation models of natural gas reservoirs with high-temperature and overpressure in Yinggehai Basin. Acta Pet. Sin. 33, 601–609 (in Chinese with English abstract).

Xie, Y., Zhang, Y., Xu, X., Gan, J., 2014. Natural gas origin and accumulation model in major and excellent gas fields with high temperature and overpressure in Yinggehai basin: a case of DF13-2 gasfield. China Offshore Oil and Gas 26, 1–5 (in Chinese with English abstract).

Zhang, H., Pei, J., Zhang, Y., Jiang, C., Zhu, J., Ai, N., Hu, Q., Yu, J., 2013. Overpressure reservoirs of the Huangliu Formation of the Dongfang area, Yinggehai Basin, South China Sea. Petrol. Explor. Dev. 40, 305–316.

Zhang, L.G., Qu, H.J., Chen, S., Zhou, W., Mo, F.Y., Han, X., 2021. Sedimentary characteristics and model of shallow sea sandy debrisflow: A case study of Ying Ⅱ Member in the Dongfang 1-1 Gas Field, Yinggehai Basin. Bulletin of Geological Science and Technology 40 (6), 140–150 (in Chinese with English abstract).

Zheng, F., Song, R., Dong, G., Chen, H., Wang, Y., Zhang, C., Wu, T., Zheng, H., Liang, Y., 2023. Study on present geothermal field and thermal structure in Yinggehai Basin. Journal of Chengdu University of Technology (Science & Technology Edition) 50, 661–672 (in Chinese with English abstract).

Zhou, Z., Ballentine, C.J., 2006. ^4He dating of groundwater associated with hydrocarbon reservoirs. Chem. Geol. 226, 309–327.

Zhou, Z., Ballentine, C.J., Kipfer, R., Schoell, M., Thibodeaux, S., 2005. Noble gas tracing of groundwater/coalbed methane interaction in the San Juan Basin, USA. Geochim. Cosmochim. Acta 69, 5413–5428.